PAPER • OPEN ACCESS

Femtosecond XUV–IR induced photodynamics in the methyl iodide cation

View the article online for updates and enhancements.

New Journal of Physics

The open access journal at the forefront of physics

PAPER

Femtosecond XUV–IR induced photodynamics in the methyl iodide cation

CrossMark

OPEN ACCESS

Marta L Murillo-Sánchez[1] , Geert Reitsma[2], Sonia Marggi Poullain[1,3] ,
Pedro Fernández-Milán[4], Jesús González-Vázquez[4] , Rebeca de Nalda[5] ,
Fernando Martín[4,6,7], Marc J J Vrakking[2] , Oleg Kornilov[2,*] and Luis Bañares[1,6,*]

1   Departamento de Química Física (Unidad Asociada I+D+i al CSIC), Facultad de Ciencias Químicas, Universidad Complutense de Madrid, 28040 Madrid, Spain
2   Max-Born-Institute, Max Born Strasse 2A, D-12489 Berlin, Germany
3   Department of Chemistry, University of California, Berkeley, California 94720, United States of America
4   Departamento de Química, Módulo 13, Facultad de Ciencias, Universidad Autónoma de Madrid, 28049 Madrid, Spain
5   Instituto de Química Física Rocasolano, Consejo Superior de Investigaciones Científicas, Serrano 119, 28006 Madrid, Spain
6   Instituto Madrileño de Estudios Avanzados en Nanociencia (IMDEA-Nanoscience), Cantoblanco, 28049 Madrid, Spain
7   Condensed Matter Physics Center (IFIMAC), Universidad Autónoma de Madrid, 28049 Madrid, Spain
*   Authors to whom any correspondence should be addressed.

E-mail: oleg.kornilov@mbi-berlin.de and lbanares@ucm.es

Abstract

The time-resolved photodynamics of the methyl iodide cation (CH_3I^+) are investigated by means of femtosecond XUV–IR pump–probe spectroscopy. A time-delay-compensated XUV monochromator is employed to isolate a specific harmonic, the 9th harmonic of the fundamental 800 nm (13.95 eV, 88.89 nm), which is used as a pump pulse to prepare the cation in several electronic states. A time-delayed IR probe pulse is used to probe the dissociative dynamics on the first excited $\widetilde{A}\ ^2A_1$ state potential energy surface. Photoelectrons and photofragment ions—CH_3^+ and I^+—are detected by velocity map imaging. The experimental results are complemented with high level *ab initio* calculations for the potential energy curves of the electronic states of CH_3I^+ as well as with full dimension on-the-fly trajectory calculations on the first electronically excited state $\widetilde{A}\ ^2A_1$, considering the presence of the IR pulse. The CH_3^+ and I^+ pump–probe transients reflect the role of the IR pulse in controlling the photodynamics of CH_3I^+ in the $\widetilde{A}\ ^2A_1$ state, mainly through the coupling to the ground state $\widetilde{X}\ ^2E_{3/2,1/2}$ and to the excited $\widetilde{B}\ ^2E$ state manifold.

Oscillatory features are observed and attributed to a vibrational wave packet prepared in the $\widetilde{A}\ ^2A_1$ state. The IR probe pulse induces a coupling between electronic states leading to a slow depletion of CH_3^+ fragments after the cation is transferred to the ground $\widetilde{X}\ ^2E_{3/2,1/2}$ states and an enhancement of I^+ fragments by absorption of IR photons yielding dissociative photoionization.

1. Introduction

Methyl iodide has served for many years as a prototypical system for a variety of studies of photoinduced dynamics, from its photodissociation in the first absorption band (see, for instance, references [1–5]) to x-ray photoabsorption-induced charge transfer [6–8] among others. Its photoionization into CH_3I^+ and the subsequent dissociation has been actively investigated in particular employing multiphoton strong-field excitation [9–20]. In such studies, intense IR femtosecond pulses have been often used to ionize the molecule leading eventually to dissociative photoionization (DPI) as well as to Coulomb explosion (CE) producing charged methyl and iodine fragments. Such an approach leads to a large number of reaction pathways and fragments, and hence to a challenging interpretation. The goal, here, is to employ an extreme ultraviolet (XUV) pump—infrared (IR) probe scheme with femtosecond time resolution to demonstrate how a moderately strong IR pulse can control and modify the photodynamics following one-photon XUV

ionization into CH_3I^+. The present experiments allow us to largely reduce the number of opened dissociation channels and thus to get a deeper understanding of the induced photodynamics of CH_3I^+.

The methyl iodide cation (CH_3I^+) is characterized by a bound ground electronic state with two spin–orbit components $\widetilde{X}$ $^2E_{3/2}$ and $\widetilde{X}$ $^2E_{1/2}$, with ionization thresholds of 9.54 and 10.168 eV, respectively [21–23]. The first excited state $\widetilde{A}$ $^2A_1$, whose band origin is located at 11.9 eV [24], is loosely bound. Its rovibrational structure, which has been studied by high resolution photoelectron spectroscopy [21] and several photoionization studies [24–27], reveals vibrational progressions dominated by the ν_3 mode (C–I stretch), superimposed on the ν_1 (symmetric C–H stretch) and ν_2 (umbrella) normal modes. In contrast, the second band, lying between 14 and 16 eV, is assigned to the $\widetilde{B}$ ^2E excited repulsive state, although recently computed potential energy curves (PECs) show rather a manifold of repulsive states corresponding to this band [28].

Dissociative photoionization involving the $\widetilde{X}$, $\widetilde{A}$ and $\widetilde{B}$ ionic states can lead to either $CH_3^+ + I$ or $CH_3 + I^+$ fragment channels, characterized by appearance energies 12.2 and 12.9 eV, respectively [29]. Early photoelectron photoion coincidence (PEPICO) studies of one photon-ionization into the $\widetilde{A}$ state observed a statistical dissociation leading to the formation of the CH_3^+ fragment with a small amount of translational energy [30–32]. Experiments employing velocity map imaging (VMI) in combination with multiphoton strong-field excitation using femtosecond IR pulses have been later reported, including some investigations on the dependence of the dynamics on the IR intensity [11, 12, 14]. The different reaction pathways through DPI and CE leading to charged methyl and iodine fragments are discussed based on the images and in particular, dissociation from the $\widetilde{A}$ excited state is suggested to occur through internal conversion to the ground state CH_3I^+, while direct dissociation in the $\widetilde{B}$ state is also observed. Further investigations are focused on the angular distributions and measurements of photoemission asymmetries employing well-aligned molecules or phase-controlled two-color laser fields, where the results are rationalized in terms of the symmetry of the ionized orbitals involved [9, 13, 17–19].

More recently, femtosecond XUV absorption spectroscopy was employed by Wei *et al* to investigate strong-field induced dynamics of CH_3I^+ via multiphoton excitation using few-cycle (6 fs) IR pulses centered at 786 nm and with a peak intensity of 1.9×10^{14} W cm^{-2} [15, 16]. Besides multimode vibrational coherences observed in the populated cationic state, a selective dissociation through one of the spin–orbit components of the ground state of the cation was observed. According to Wei *et al*, such selective coupling seems to vanish when intense laser pulses of longer duration are employed as revealed by previous strong-field experiments performed by Tang and co-workers using reflectron time-of-flight mass spectrometry (RETOF-MS) with $\approx$100 fs pulses [10].

Time-resolved coincident ion momentum imaging (COLTRIMS) experiments were also recently reported by Rudenko and co-workers [20]. An IR pump pulse of 25 fs duration centered at 790 nm and with a peak intensity of $1.5–4 \times 10^{14}$ W cm^{-2} was employed to strong field ionize methyl iodide, mostly into the $\widetilde{A}$ $^2A_1$ state. At varying time delays, a second IR pulse of the same intensity was used to probe the dynamics by CE imaging. While different dissociative ionization pathways were discussed, oscillatory features, characterized by a 130 fs periodicity and dephasing within 1 ps, were observed and assigned to a vibrational wave packet in the C–I symmetric stretch ν_3 mode moving in the $\widetilde{A}$ $^2A_1$ state of CH_3I^+.

In the present study, we take advantage of the development of high harmonic generation (HHG)-based XUV sources to study the time-resolved dissociation of the methyl iodide cation prepared in electronically excited states, and, in particular, the role of a time-delayed moderately strong IR probe pulse on the electronic and vibrational dynamics. A time-delay-compensated XUV monochromator [33, 34] is employed to isolate specific harmonics for one-photon ionizing the methyl iodide molecule, allowing the preparation of a well-defined mixture of ionic states, while VMI is employed to detect selected fragment ions—in particular CH_3^+ and I^+—as well as photoelectrons. The ground $\widetilde{X}$ $^2E_{3/2,1/2}$ and excited $\widetilde{A}$ $^2A_1$ states of CH_3I^+ are populated using the 9th harmonic of the fundamental 800 nm (13.95 eV, 88.89 nm), the latter leading to CH_3^+ and I^+ fragments through different dissociation pathways which are strongly modified by the IR probe femtosecond pulse. The experimental results are complemented by high level *ab initio* calculations of the PECs, in combination with full dimension on-the-fly trajectory calculations on the $\widetilde{A}$ $^2A_1$ state in the absence and presence of the IR pulse. The combined experimental and theoretical results provide a detailed picture of the CH_3I^+ dissociation and the action mechanisms of the IR probe pulse. The experimental and theoretical methodologies are described in section 2, while the experimental and theoretical results are presented and discussed in section 3, including the photoelectron spectra, the kinetic energy release distributions for the CH_3^+ and I^+ fragments as a function of the XUV–IR delay time and the corresponding XUV–IR pump–probe transients. The main conclusions are summarized in section 4.
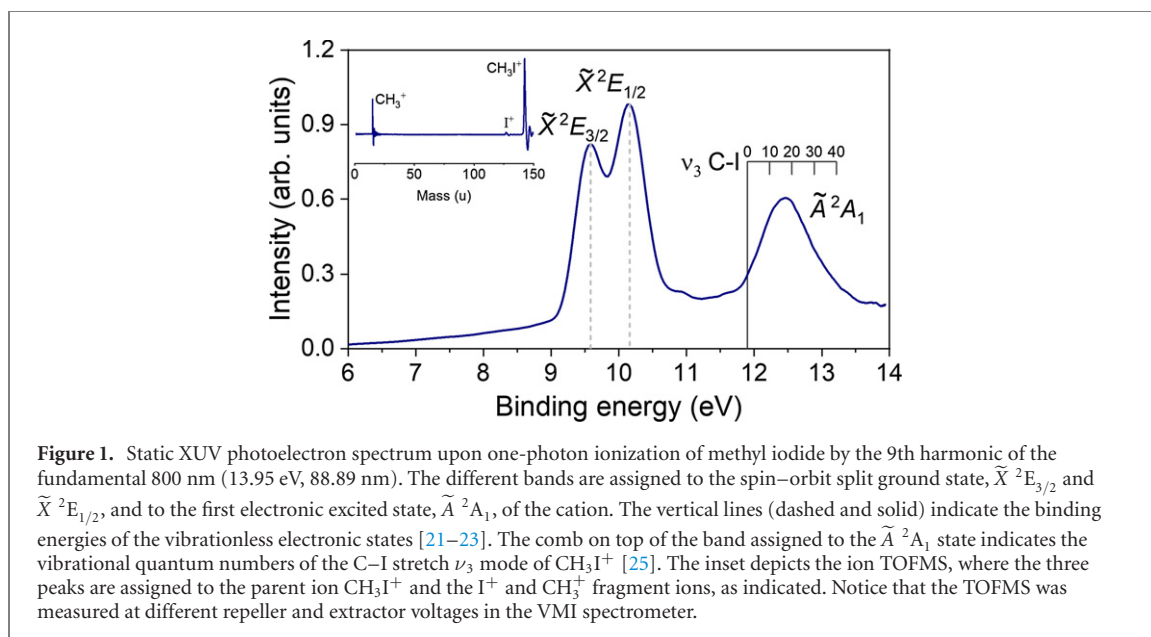
2. Methods

2.1. Experiment

The experimental setup has been described in detail in reference [33]. In brief, a commercial Ti:Sapphire laser system (Aurora, Amplitude Technologies) delivers 5 mJ (up to 20 mJ) pulses of 25 fs duration at 1 kHz repetition rate with a tunable central wavelength of about 800 nm. The pulses are equally split between the pump (XUV) and probe (IR) arms of the setup. The pump beam is focused by a concave spherical mirror (focal length of 62.5 cm) into a gas cell situated in a vacuum chamber and filled with Kr to a pressure of 45 mbar. The generating IR pulses are separated from the XUV pulses by a 100 nm thin Al filter. The XUV pulse is wavelength-selected by a time-delay-compensated monochromator (TDCM) with a spectral resolution of 300 meV and an output pulse duration of 20–25 fs [33]. The other part of the IR beam is split before the TDCM and used as a probe beam. Both beams are recombined after the TDCM and focused into the interaction region of a VMI spectrometer [35]. The sample, in this case methyl iodide, is introduced into the interaction region via a 150 μm orifice in the VMI repeller electrode, which allows to achieve high target densities at the focus of the XUV and IR pulses and to compensate the low flux of the XUV photons [35]. Both photoelectrons and photoions can be detected by changing the electrodes' (both repeller and extractor) polarity. Typical voltages are 2 kV and 1.9 kV for the repeller and extractor plates, respectively. A voltage scheme is applied to the microchannel plates (MCP) detector to select specific fragment ions based on their time-of-flight (TOF). Static photoelectron VMI images were measured using the 9th harmonic of the fundamental 800 nm (13.95 eV, 88.89 nm). Time-dependent XUV–IR pump–probe photoion VMI images were then acquired detecting the CH_3^+ and I^+ fragments in separate experimental runs. The time delay scans were run from −1000 fs to 1000 fs in 13 fs steps and repeated multiple times forward and backward for each fragment. In all time axes in this work, a positive time-delay means that the IR comes after XUV.

To establish the time resolution of the experiment, the XUV–IR cross-correlation was measured by generating sidebands of photoionization lines in Ar, which are only present if both XUV and IR pulses are spatially and temporally overlapped [36–38]. The XUV–IR cross-correlation was first optimized by tuning the femtosecond pulse chirp using an acousto-optic programmable dispersive filter (Dazzler, Fastlite) to independently maximize the above-threshold ionization in Ar (IR probe beam) and the high harmonics generation (XUV pump beam). The resulting difference of the optimal second order dispersion between the two arms was compensated by adding fused silica plates to the NIR beam generating the XUV pulses. The cross-correlation signal was well reproduced by a Gaussian profile with a full-width-at-half-maximum (FWHM) of 36 ± 5 fs. The VMI spectrometer was calibrated by recording vibrationally resolved VMI images of N_2^+ predissociation in the $\widetilde{C}$ state. The dissociation energy and the energies of the vibrational states of $N_2^+(\widetilde{C})$ were adopted from references [39, 40], respectively. The intensity of the IR probe pulse was estimated [38] to be 1.3×10^{13} W cm^{-2} and was maintained at this moderate level on purpose to avoid strong multiphoton absorption and multiple ionization leading to CE of CH_3I molecules.

2.2. Theoretical methods

In order to characterize the electronic structure of the methyl iodide cation, several electronic states were calculated using multireference methods based on state-averaged CASSCF wavefunctions. Relativistic effects were taken into account by using a second order Douglas–Kroll Hamiltonian [41, 42] formalism in combination with the ANO-RCC [43, 44] basis set contracted to a triple zeta polarized (ANO-RCC-TZVP) basis set. The two electron integrals were evaluated using the density fitting approximation [45] where the selected auxiliary basis set was constructed using the uncontracted ANO-RCC basis. The active space used in the CASSCF calculations is composed of 6 electrons in 4 orbitals. Specifically, the set of orbitals considered in this study contains two lone pairs of the iodine atom, σ_{CI}-bonding and σ_{CI}-antibonding. Two sets of orbitals were obtained using the state averaging technique, the first one taking into account 11 doublets and the second one averaging over 3 quadruplets. Finally, the energy was corrected by perturbation theory in its extended multi-state CASPT2 (XMS-CASPT2) formalism [46] with an imaginary shift of 0.3. These calculations were performed using the BAGEL code [47], including analytical gradients [48–50] when required. Finally, spin–orbit coupling (SOC) was taken into account using the AMFI approximation [51], resulting in a total of 36 electronic states. This calculation was performed by extracting the CASSCF wavefunction—configuration interaction (CI) vector and orbitals—from the BAGEL code and importing it into the OpenMolcas code [52], where the SOC coupling was evaluated using a perturbation modified approximation (PM-CASSCF). The number of calculated states was selected to describe correctly the dissociation limits of the first five channels: $CH_3^+ + I(^2P_{3/2})$; $CH_3 + I^+(^3P_2)$; $CH_3^+ + I(^2P_{1/2})$; $CH_3 + I^+(^3P_0)$; and $CH_3 + I^+(^3P_1)$, similarly to reference [28]. In order to estimate the reliability of the method (especially the selection of the auxiliary basis set), the electronic energies were evaluated as a function of the

Figure 1. Static XUV photoelectron spectrum upon one-photon ionization of methyl iodide by the 9th harmonic of the fundamental 800 nm (13.95 eV, 88.89 nm). The different bands are assigned to the spin–orbit split ground state, $\widetilde{X}\ ^2E_{3/2}$ and $\widetilde{X}\ ^2E_{1/2}$, and to the first electronic excited state, $\widetilde{A}\ ^2A_1$, of the cation. The vertical lines (dashed and solid) indicate the binding energies of the vibrationless electronic states [21–23]. The comb on top of the band assigned to the $\widetilde{A}\ ^2A_1$ state indicates the vibrational quantum numbers of the C–I stretch ν_3 mode of CH_3I^+ [25]. The inset depicts the ion TOFMS, where the three peaks are assigned to the parent ion CH_3I^+ and the I^+ and CH_3^+ fragment ions, as indicated. Notice that the TOFMS was measured at different repeller and extractor voltages in the VMI spectrometer.

C–I distance. In this case, a relaxed curve was calculated using the external optimizer of ORCA [53] in combination with the analytical gradients and SOC described before, where the methyl moiety was optimized in its spin-free doublet ground cationic state with XMS-CASPT2, i.e. the gradients obtained with BAGEL were passed to the ORCA program to optimize the molecule with constrained C–I distance.
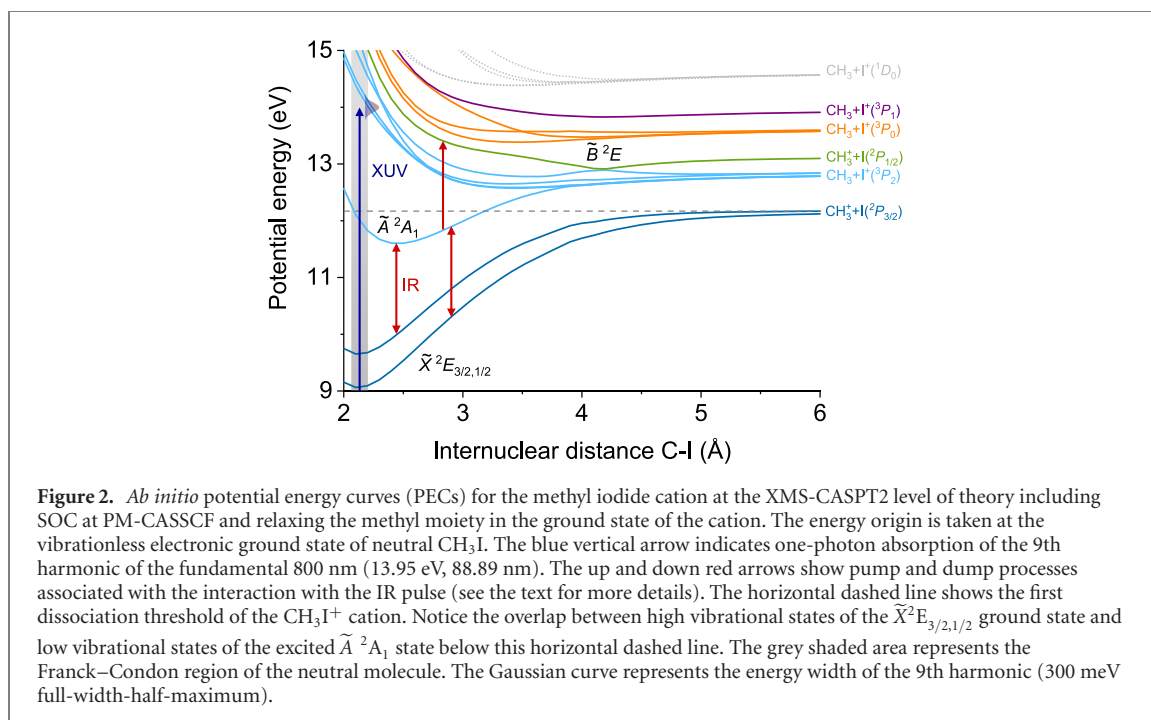
A set of initial geometries and velocities was obtained considering the Hessian of an MP2 optimization, using a Wigner distribution in Cartesian coordinates based on the harmonic approximation with an open-source code [54]. For each geometry, the Dyson norm was also evaluated using the OpenMolcas code [52] in its spin–orbit variant. As in the previous case, the wavefunction and energies were evaluated using the XMS-CASPT2 method and the same PM-CASSCF formalism was employed to calculate the Dyson orbitals. Additionally, the calculation of the Dyson orbitals required to obtain a neutral initial state that was represented coupling 3 singlet and 3 triplet states, in the same way as for the cationic states. The dynamics of the cation (including 40 trajectories) was performed using the SHARC method [55], where the Hamiltonian and the spin-free gradients were described using the previous electronic structure protocol and the surface hopping probability was evaluated based on the variation of the densities [56].

Finally, the effect of the probe IR pulse was simulated selecting the geometries of the trajectories at given times and propagating the electronic time-dependent Schrödinger equation with the split-operator technique [57–59], where the diagonal elements of the electronic Hamiltonian (obtained at the different geometries) are the XMS-CASPT2 energies, whereas the off-diagonal elements are the SOC values obtained at PM-CASSCF level. The laser pulse interaction was described within the dipole approximation in the length gauge with PM-CASSCF. Specifically, truncated sine square laser pulses with frequency corresponding to 800 nm, amplitudes from 5.3×10^{-3} a.u. up to 1.69×10^{-2} a.u.—equivalent to intensities in the range 0.98–10 TW cm^{-2}, and time duration of 15 fs (FWHM), were employed.

3. Results and discussion

3.1. Static XUV photoelectron spectra and photoion mass spectra

Figure 1 shows the static XUV photoelectron spectrum (PES) along with the corresponding ion time-of-flight mass spectrum (TOFMS) measured by one-photon XUV ionization of CH_3I using the 9th harmonic of the fundamental 800 nm (13.95 eV, 88.89 nm). The bands observed in the PES are assigned to the different electronic states in which the CH_3I^+ is prepared after photoionization at 13.95 eV. The low binding energy bands at 9.45 and 10.2 eV correspond to the spin–orbit split ground state ($\widetilde{X}\ ^2E_{3/2}$ and $\widetilde{X}\ ^2E_{1/2}$) and the broad band at larger binding energy is assigned to the first excited state ($\widetilde{A}\ ^2A_1$). The internal energy content of the cation prepared in the $\widetilde{A}\ ^2A_1$ state is considered, by calculating the binding energies corresponding to the vibrational states in the C–I stretch ν_3 mode. Accordingly, the cation is prepared in this state with a significant vibrational excitation with the distribution peaking at ν_3 mode quantum numbers of about 15. This distribution of vibrational states in the $CH_3I^+(\widetilde{A}\ ^2A_1)$ state is very similar to the Franck–Condon vibrational state distribution calculated by Malakar *et al* [20].

Figure 2. *Ab initio* potential energy curves (PECs) for the methyl iodide cation at the XMS-CASPT2 level of theory including SOC at PM-CASSCF and relaxing the methyl moiety in the ground state of the cation. The energy origin is taken at the vibrationless electronic ground state of neutral CH_3I. The blue vertical arrow indicates one-photon absorption of the 9th harmonic of the fundamental 800 nm (13.95 eV, 88.89 nm). The up and down red arrows show pump and dump processes associated with the interaction with the IR pulse (see the text for more details). The horizontal dashed line shows the first dissociation threshold of the CH_3I^+ cation. Notice the overlap between high vibrational states of the $\widetilde{X}^2E_{3/2,1/2}$ ground state and low vibrational states of the excited $\widetilde{A}\ ^2A_1$ state below this horizontal dashed line. The grey shaded area represents the Franck–Condon region of the neutral molecule. The Gaussian curve represents the energy width of the 9th harmonic (300 meV full-width-half-maximum).

The measured PES can be well understood by using the calculated PECs in C_s symmetry along the C–I dissociative coordinate for the first electronic states of CH_3I^+ depicted in figure 2. The spin–orbit ground states of the cation, $^2E_{3/2}$ and $^2E_{1/2}$, correlate with the $CH_3^+ + I(^2P_{3/2})$ fragments which appear at the first dissociation limit at 12.29 eV, while the loosely bound first excited electronic state $\widetilde{A}^2A_1$ correlates with the $CH_3 + I^+(^3P_2)$ fragments appearing at 12.95 eV. In this 1D calculation, the PECs correlating with the two first dissociation limits are well separated at every C–I distance. At higher energies, repulsive PECs corresponding to the $\widetilde{B}$ band are observed, correlating with the $CH_3 + I^+(^3P_2)$ and $CH_3^+ + I(^2P_{1/2})$ asymptotes, as well as to higher energy channels yielding neutral CH_3 fragments in combination with different electronic states of the ionized iodine fragment, $I^+(^3P_0)$ and $I^+(^3P_1)$. The first three dissociation limits computed here at CASPT2 level of theory—12.09, 12.95 and 13.05 eV—are in good agreement with the experimental values of 12.18, 12.90 and 13.12 eV [11].

The ion TOFMS depicted in the inset of figure 1 shows three peaks which are assigned to the parent ion CH_3I^+ and the fragment ions I^+ and CH_3^+, the intensity of the latter being substantially larger than that of the former. Considering the low intensity of the XUV pulses, the XUV ionization is restricted to one-photon ionization and, thus, the presence of the fragment ions in the mass spectrum indicates dissociation of CH_3I^+. In agreement with the previous work [30–32], the I^+ fragments are produced in direct dissociation from the $\widetilde{A}\ ^2A_1$ state. The presence of CH_3^+ fragments in the TOFMS can be explained by dissociation on the $\widetilde{X}\ ^2E_{3/2,1/2}$ ground state following curve crossing from the $\widetilde{A}\ ^2A_1$ state. Actually, C–I stretch ν_3 vibrational states in the $\widetilde{A}\ ^2A_1$ state with quantum numbers larger than 10 are above the lowest dissociation limit $CH_3^+ + I(^2P_{3/2})$. The coupling between the vibrational continuum of $\widetilde{X}\ ^2E_{3/2,1/2}$ and the initially populated $\widetilde{A}\ ^2A_1$ state leads to the non-adiabatic crossing and the cation dissociates in the ground state yielding CH_3^+ fragment ions.

A semiclassical simulation of the static XUV PES was performed using the norm of the Dyson orbitals for each of a total of 200 geometries forming a Wigner distribution in the vibrational ground state of the neutral CH_3I ($\widetilde{X}\ A_1$). The resulting ionization probability, convoluted with a Gaussian function of 0.3 eV width, is depicted in figure 3(a) as a function of the ionization energy, i.e. the energy difference between the ionic state and the initial energy of the CH_3I ($\widetilde{X}\ A_1$) ground state. Three bands are observed, located at similar positions as the ionization energies (vertical bars) calculated at the Frank–Condon geometry, i.e. 9.22 eV, 9.81 eV and 12.34 eV, respectively. Similar to the experiment (see figure 1), the lower ionization energy bands correspond to the spin–orbit split ground state ($\widetilde{X}\ ^2E_{3/2}$ and $\widetilde{X}\ ^2E_{1/2}$) of the cation, while the band at larger ionization energy corresponds to the first excited state of the cation ($\widetilde{A}\ ^2A_1$). This third band spreads out over a larger energy range, although it remains considerably narrower than the one observed experimentally, due to the lack of quantization in the vibrational modes in the present semiclassical simulation. No appreciable contribution is observed for the second excited state of the cation ($\widetilde{B}\ ^2E$), which
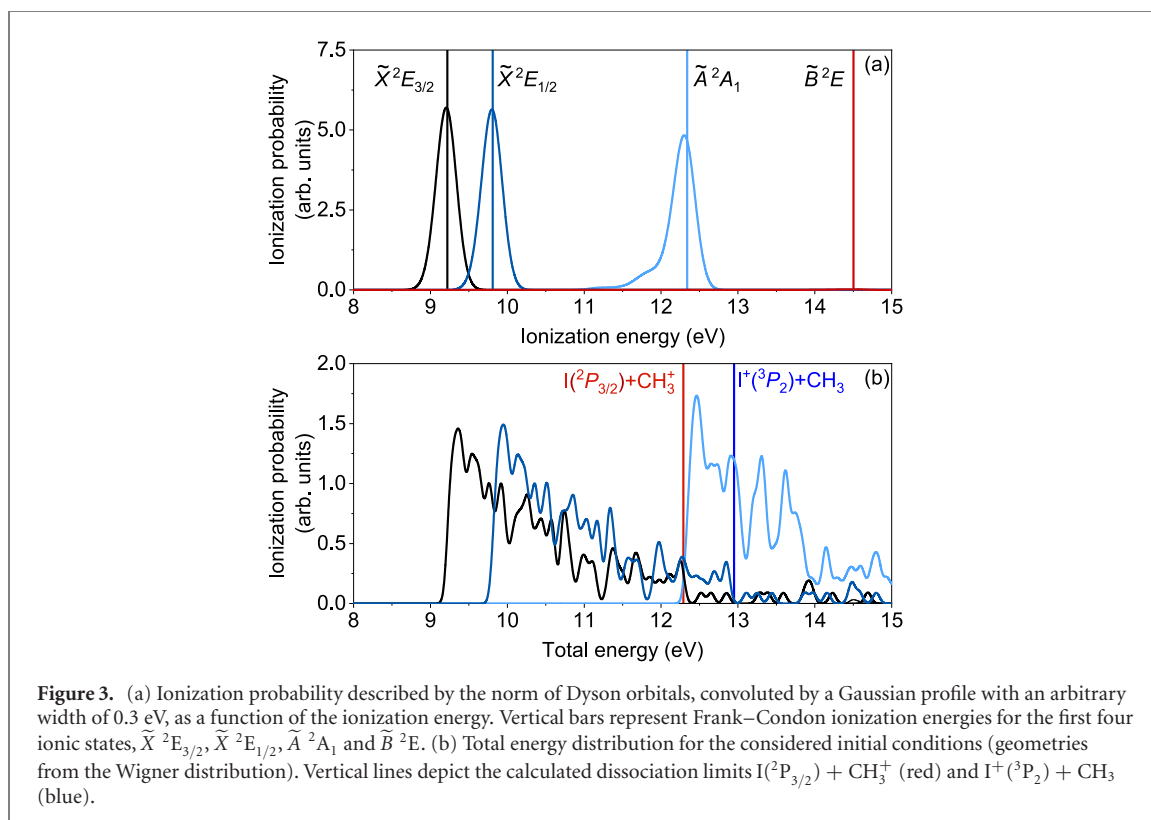
Figure 3. (a) Ionization probability described by the norm of Dyson orbitals, convoluted by a Gaussian profile with an arbitrary width of 0.3 eV, as a function of the ionization energy. Vertical bars represent Frank–Condon ionization energies for the first four ionic states, $\widetilde{X}\ ^2E_{3/2}$, $\widetilde{X}\ ^2E_{1/2}$, $\widetilde{A}\ ^2A_1$ and $\widetilde{B}\ ^2E$. (b) Total energy distribution for the considered initial conditions (geometries from the Wigner distribution). Vertical lines depict the calculated dissociation limits $I(^2P_{3/2}) + CH_3^+$ (red) and $I^+(^3P_2) + CH_3$ (blue).

should appear at 14.50 eV. The geometries from the Wigner distribution, distributed on the ionic states, constitute in general the initial conditions employed to carry out full-dimension trajectory calculations.

Figure 3(b) represents the total energy distribution for each of the three ionic states for all initial conditions (geometries from the Wigner distribution). The abscissa axis represents the total energy with respect to the minimum energy of the neutral molecule in its ground state. This total energy includes the potential energy of the cationic state and the kinetic energy initially present in the ground state of the neutral molecule. The total energy distribution shows three asymmetric broad bands reflecting the broad contribution of kinetic energies. Vertical bars correspond to the two first dissociation limits $I(^2P_{3/2}) + CH_3^+$ and $I^+(^3P_2) + CH_3$ calculated at 12.17 and 12.82 eV, respectively. As observed, the third state of the cation ($\widetilde{A}\ ^2A_1$) can dissociate into CH_3 and $I^+(^3P_2)$. In contrast, dissociation from the two first ionic states ($\widetilde{X}\ ^2E_{3/2}$ and $\widetilde{X}\ ^2E_{1/2}$) is very unlikely, and only a very small fraction can dissociate into the first dissociation limit.
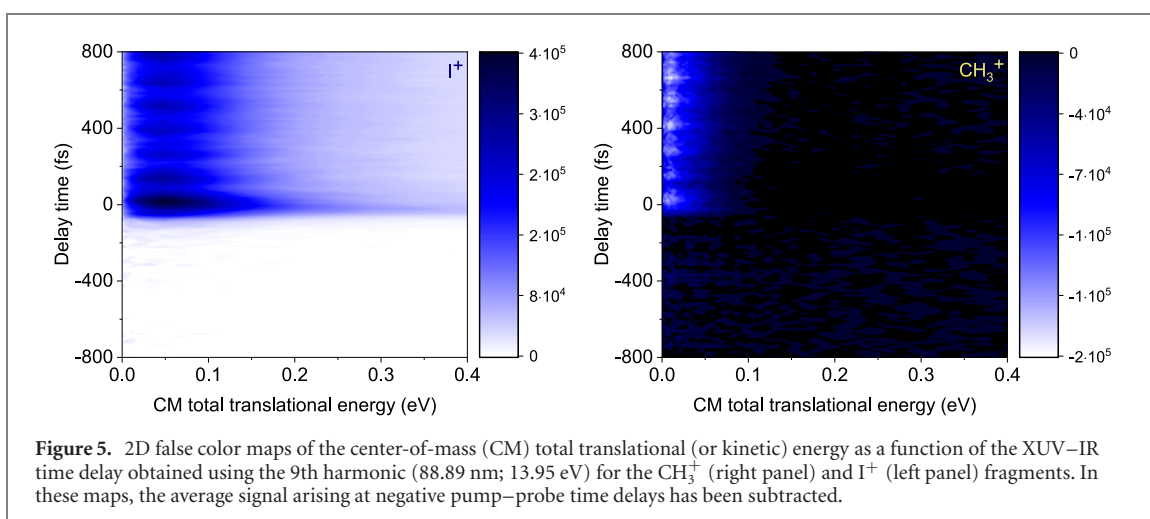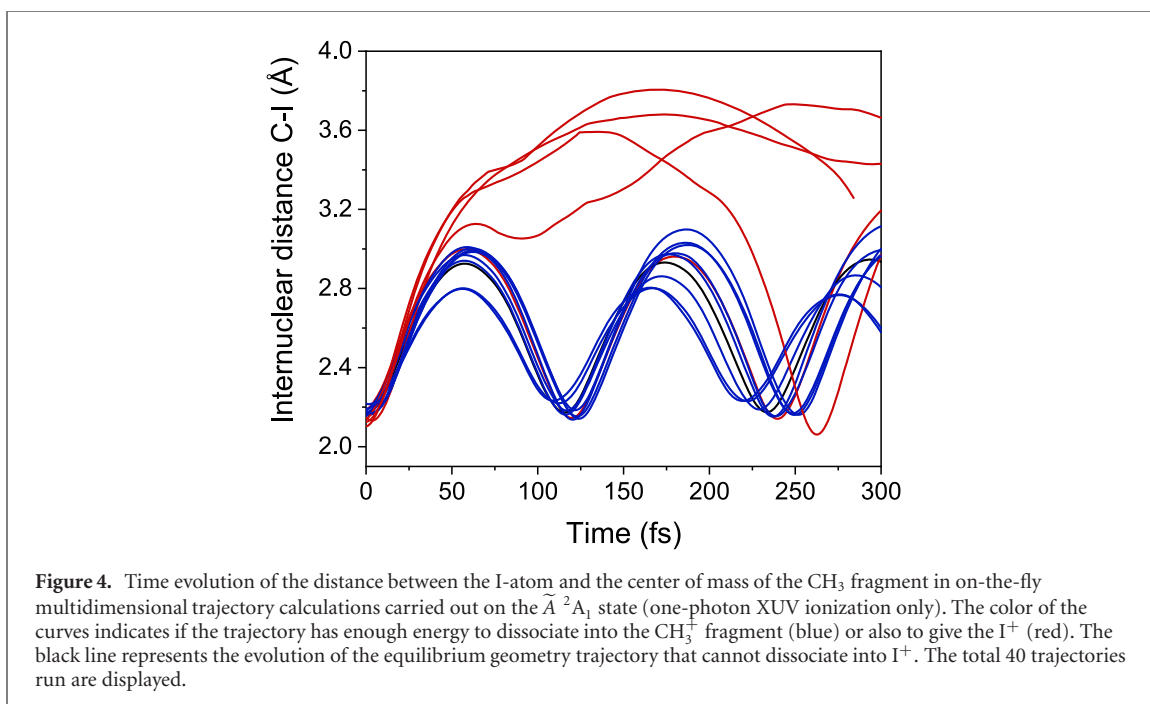
Figure 4 depicts the results of on-the-fly multidimensional trajectory calculations carried out on the $\widetilde{A}\ ^2A_1$ state, which help to assess the dynamics upon one-photon XUV ionization. As can be seen most of the trajectories remain trapped in the potential well (blue lines), while a minor number of them seem to have enough energy to directly dissociate into I^+ (red lines).

3.2. Fragment translational energy distributions and XUV–IR transients

XUV pump–IR probe experiments were performed for the 9th harmonic of the fundamental 800 nm (13.95 eV, 88.89 nm). Velocity map images for both the CH_3^+ and I^+ fragments have been measured as a function of the XUV–IR time delay. Figure 5 displays 2D false color maps of the total kinetic energy release (TKER) as a function of time delay extracted from the VMI images of the CH_3^+ and I^+ fragment ions.

The 2D maps feature only low TKER contributions for both fragment ions. Some common features can be identified in the two maps. In particular, there is only time-dependent signal for positive pump–probe time delays, i.e. when the XUV pulse arrives first. Oscillatory structures in the TKERs ranging from zero up to about 0.06–0.08 eV for the CH_3^+ fragment and from zero up to 0.12–0.15 eV for the I^+ fragment are clearly observed. Interestingly, whereas the yield of the I^+ fragment increases with the time delay, the CH_3^+ fragment yield is depleted. Due to the low TKER of the fragments, it is not possible to extract confidently the angular distributions and thus to obtain the corresponding anisotropy parameter, β.

The integration of the signal in the 2D maps in the region of translational energy of interest vs time delay leads to the transients depicted in figure 6, which confirm the enhanced signal for the I^+ fragment and the depleted signal for the CH_3^+ fragment. The analysis of the I^+ transient is carried out by three

Figure 4. Time evolution of the distance between the I-atom and the center of mass of the CH$_3$ fragment in on-the-fly multidimensional trajectory calculations carried out on the $\widetilde{A}\ ^2A_1$ state (one-photon XUV ionization only). The color of the curves indicates if the trajectory has enough energy to dissociate into the CH$_3^+$ fragment (blue) or also to give the I$^+$ (red). The black line represents the evolution of the equilibrium geometry trajectory that cannot dissociate into I$^+$. The total 40 trajectories run are displayed.

Figure 5. 2D false color maps of the center-of-mass (CM) total translational (or kinetic) energy as a function of the XUV−IR time delay obtained using the 9th harmonic (88.89 nm; 13.95 eV) for the CH$_3^+$ (right panel) and I$^+$ (left panel) fragments. In these maps, the average signal arising at negative pump−probe time delays has been subtracted.

contributions to the data: an exponential decay τ_1, an exponential rise τ_2 and a damped oscillation with a period T, according to

$$S = \Theta(t) \left[A\,e^{-t/\tau_1} + B(1 - e^{-t/\tau_2}) + C(1 + D\cos(2\pi t/T + \phi))\,e^{-t/\tau_2} \right] \times g_{cc}(t), \tag{1}$$

where $\Theta(t)$ is a step function and the expression is convoluted with the apparatus cross-correlation function $g_{cc}(t)$ assumed to have a Gaussian profile. A, B, C and D are amplitude coefficients of the different contributions. In the fit we assume that the damping rate of the oscillation is the same as the time constant of the exponential rise. The reason for this restriction is discussed below. The fit results are depicted in figure 6 by dashed curves. The overall fit for both fragments recovers all the features observed in the experimental transient. In the case of the CH$_3^+$ transient, the data are fitted using the same expression, but owing to the stronger noise in this transient, the decay constants τ_1 and τ_2 are fixed to the values obtained from the fit of the I$^+$ transient. Table 1 shows the time constants obtained from the fits of the I$^+$ and CH$_3^+$ transients.

As commented on in the previous section, according to the photoelectron and TOFMS depicted in figure 1, the 9th harmonic XUV pulse prepares the molecular cation in low vibrational states of the $\widetilde{X}\ ^2E_{1/2,3/2}$ electronic ground states, as well as in highly vibrationally excited states of the $\widetilde{A}\ ^2A_1$ state. No further dynamics and fragmentation are expected from the ionic $\widetilde{X}\ ^2E_{1/2,3/2}$ states and most of the cations prepared in the excited $\widetilde{A}\ ^2A_1$ state also remain trapped in the potential well as a vibrational wave packet
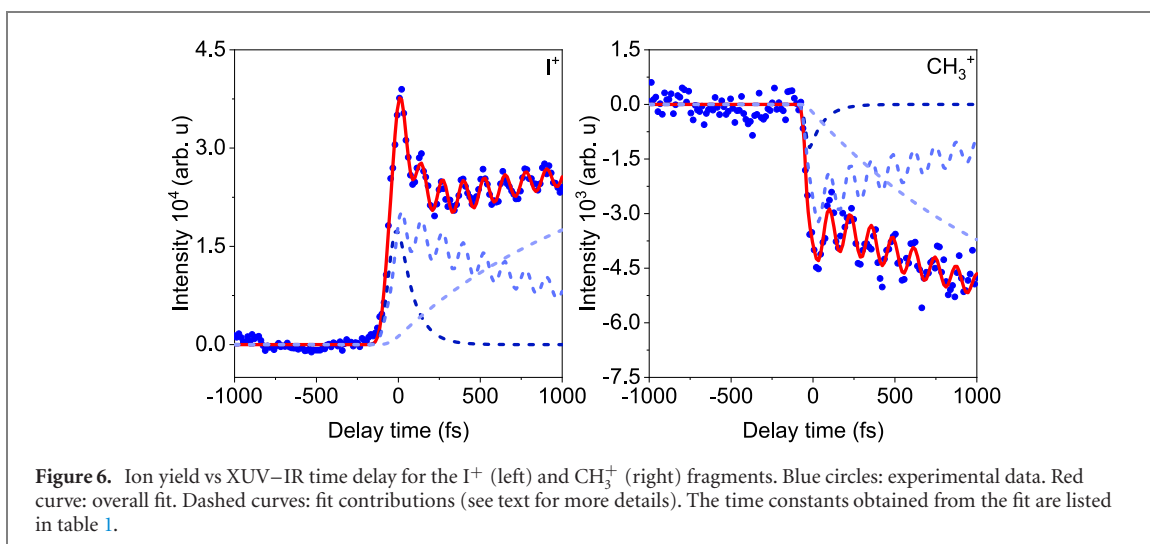
Figure 6. Ion yield vs XUV–IR time delay for the I$^+$ (left) and CH$_3^+$ (right) fragments. Blue circles: experimental data. Red curve: overall fit. Dashed curves: fit contributions (see text for more details). The time constants obtained from the fit are listed in table 1.

Table 1. Time constants τ_1, τ_2 and T (in fs) with error bars ($1 - \sigma$) obtained from the fit of the experimental transients for the two fragment ions I$^+$ and CH$_3^+$.

Transient	I$^+$	CH$_3^+$
τ_1	89 ± 12	89 (fixed)
τ_2	1300 ± 400	1300 (fixed)
T	127 ± 1	129 ± 1

(see figure 4). However, this vibrational wave packet can escape the shallow well, in principle, via two alternative routes: a minor part can directly dissociate into CH$_3$ + I$^+$(^{3}P$_2$), while a major part can relax by internal conversion to the vibrational continuum of the spin–orbit split ground state of the cation $\widetilde{X}$ ^{2}E$_{3/2,1/2}$, where it dissociates yielding CH$_3^+$ + I(^{2}P$_{3/2}$) with low kinetic energy. This dissociation pathway was suggested in early photoionization work [30].

When we consider the 2D maps and transients showing the XUV–IR pump–probe data depicted in figures 5 and 6, we can assign the oscillatory time-dependent signal for the I$^+$ fragment to dynamics occurring on the excited $\widetilde{A}$ ^{2}A$_1$ state. The vibrational wave packet launched by the XUV pulse is probed by the IR pulse by a one-photon transition from the $\widetilde{A}$ ^{2}A$_1$ state to a repulsive $\widetilde{B}$ ^{2}E state correlating with the CH$_3$ + I$^+$(^{3}P$_2$) asymptote. The low translational energy of the fragment ions can be explained by the fact that the $\widetilde{A}$–$\widetilde{B}$ transition occurs at C–I distances beyond the Franck–Condon region while the vibrational wave packet propagates outwards on the $\widetilde{A}$ ^{2}A$_1$ state potential energy surface. This assignment is supported by the time constant for the vibrational wave packet period $T = 127 \pm 1$ fs extracted from the fit, which is in very good agreement with the oscillatory behavior observed by Malakar *et al* in their multiphoton IR–IR pump–probe experiment [20]. The fast exponential decay component with the time constant $\tau_1 = 89 \pm 12$ fs can be assumed to correspond to direct dissociation on the excited PEC.

Additionally, the I$^+$ transient shows an exponential rise on top of the oscillatory behavior with a time constant of $\tau_2 = 1.3 \pm 0.4$ ps. We suggest that this exponential rise reflects the dynamics of the internal conversion process from the $\widetilde{A}$ to the $\widetilde{X}$ states. The population transferred to the spin–orbit $\widetilde{X}$ ^{2}E$_{3/2,1/2}$ states is probed by the IR pulse through a transition back to the $\widetilde{A}$ state, but now with the kinetic energy sufficient for direct dissociation, thus yielding an enhanced signal for I$^+$. According to this assumption the oscillatory part of the signal should be damped with the same time constant τ_2. The fit of figure 6 take this assumption into account and demonstrate that it is consistent with the experimental observations.

In the case of the CH$_3^+$ time-resolved signal, similar dynamics (fast decay, picosecond rise and damped oscillation) are observed, but with opposite signs (see figure 6). This behavior can be explained by the fact that the IR pulse, by enhancing the I$^+$ formation as described, leads to a depletion of the CH$_3^+$ signal since in the absence of an IR pulse, the wave packet created in the $\widetilde{A}$ state would have evolved into CH$_3^+$.

The behavior can be described by the fact that the IR pulse transfers energy to the cation and drives the evolving wave packet towards I$^+$ fragmentation, therefore depleting the CH$_3^+$ signal.
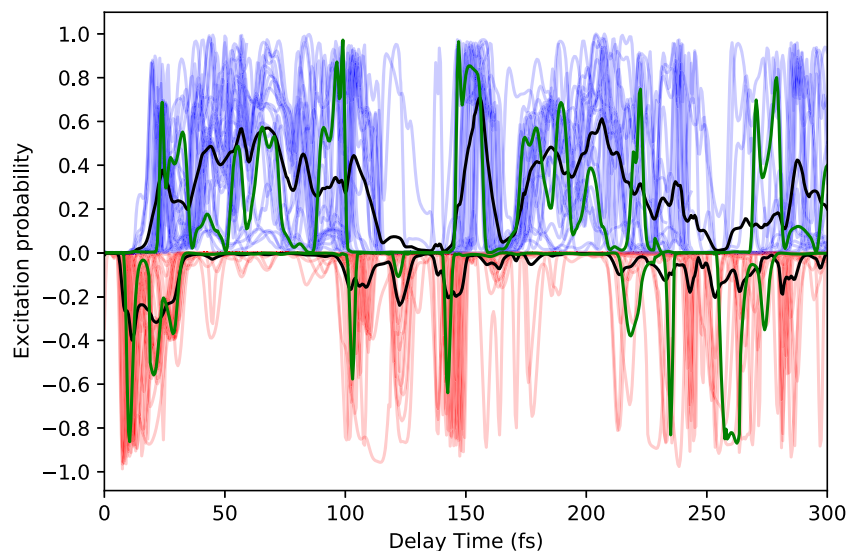
Figure 7. Population transfer from the $\widetilde{A}$-state produced by photoionization to the upper ($\widetilde{B}$, blue) and lower ($\widetilde{X}$, red) electronic states as a function of the time delay between the XUV and IR pulses. The population transfer to the lower states is plotted with negative sign (downwards) for better visibility. The probe IR pulse has an intensity of 10 TW cm^{-2}. Black line: average values of 40 trajectories. Green line: result of running the Franck–Condon geometry without initial velocity (the most probable trajectory).

3.3. The role of the IR pulse

The discussion above indicates that the IR pulse arriving after the XUV pulse can probe the dynamics on either of the two cationic states, i.e. the $\widetilde{X}\ ^2E_{1/2,3/2}$ and/or $\widetilde{A}\ ^2A_1$ states. Indeed, the IR pulse can induce three possible mechanisms: (i) a pump mechanism, where part of the wave packet trapped in the $\widetilde{A}\ ^2A_1$ state can absorb an IR photon at certain C–I distances beyond the Franck–Condon region while it is propagating outwards (i.e. at certain time delays), and then access the higher repulsive $\widetilde{B}$ state through which it quickly dissociates producing predominantly I$^+$ ions with low kinetic energy; [20] (ii) a pump mechanism from the $\widetilde{X}\ ^2E_{1/2,3/2}$ states to the $\widetilde{A}\ ^2A_1$ state, which would produce the I$^+$ fragments because of the high kinetic energy content available in the hot $\widetilde{X}\ ^2E_{1/2,3/2}$ states—and would lead to a depletion of CH$_3^+$ otherwise produced by dissociation on the $\widetilde{X}\ ^2E_{1/2,3/2}$ states-; and (iii) a dump mechanism from the $\widetilde{A}$ state down to any of the spin–orbit $\widetilde{X}$ ground states of the cation, which would not produce any fragments because the wave packet would be trapped in the deep well of the $\widetilde{X}$ states. Hence, this mechanism would not lead to any observable in the present experiment.

Figure 7 shows a simulation of the population transfer induced by the interaction of the wave packet evolving in the $\widetilde{A}\ ^2A_1$ state with the IR probe pulse, considering an intensity of 10 TW cm^{-2} for the latter. The blue curves reflect the probe process (i), where upper electronic states (from the $\widetilde{B}$-band) are populated, while the red curves reveal process (iii) (plotted with negative sign for visibility). Notice that the cross sections for mechanism (ii), i.e. the IR absorption process whereby molecules that have relaxed from the $\widetilde{A}$-state into the $\widetilde{X}$-state can be re-excited and dissociate, and mechanism (iii), i.e. the $\widetilde{A}$-to-$\widetilde{X}$ dump process, are very similar since they both involve transitions between the $\widetilde{X}\ ^2E_{1/2,3/2}$ and $\widetilde{A}\ ^2A_1$ states. Although considerably dependent on the intensity of the IR pulse, these transfers of population are highly probable at an intensity of 1.3×10^{13} W cm^{-2}, as that employed in the present experiments.

4. Conclusions

XUV–IR pump–probe experiments have been carried out to disentangle the time-resolved photoinduced dynamics of the methyl iodide cation (CH$_3$I$^+$) prepared using an XUV pulse corresponding to the 9th harmonic (13.95 eV, 88.89 nm) of a near IR pulse. One-photon XUV ionization prepares a vibrational wave packet of CH$_3$I$^+$ in the first electronically excited $\widetilde{A}\ ^2A_1$ state, where the subsequent dynamics are probed by femtosecond IR pulses. First, the time evolution of the CH$_3^+$ and I$^+$ fragments revealed by the IR pulse, shows an oscillatory behavior reflecting the evolution of a vibrational wave packet in the $\widetilde{A}\ ^2A_1$ state. Second, a fast decay in the I$^+$ transient is attributed to direct dissociation occurring adiabatically in the $\widetilde{A}\ ^2A_1$ state. Third, the slow exponential depletion in the CH$_3^+$ transient and the corresponding rise in the I$^+$ transient are assigned to the time required for internal conversion from the $\widetilde{A}$ state to the $\widetilde{X}$ ground

states of the cation. The experimental results are supported by high level *ab initio* calculations of the PECs of the electronic states of CH_3I^+ as well as by full-dimension on-the-fly trajectories on the $\widetilde{A}\ {}^2A_1$ state prepared by the XUV photon.

Acknowledgments

Data availability statement

The data that support the findings of this study are available upon reasonable request from the authors.

ORCID iDs

Marta L Murillo-Sánchez ⬚ https://orcid.org/0000-0002-9681-349X
Sonia Marggi Poullain ⬚ https://orcid.org/0000-0001-6712-3628
Jesús González-Vázquez ⬚ https://orcid.org/0000-0003-2204-3549
Rebeca de Nalda ⬚ https://orcid.org/0000-0002-9720-6106
Marc J J Vrakking ⬚ https://orcid.org/0000-0002-3249-1663
Luis Bañares ⬚ https://orcid.org/0000-0002-0777-2375

References

[1] Eppink A T J B and Parker D H 1998 Methyl iodide A-band decomposition study by photofragment velocity imaging *J. Chem. Phys.* **109** 4758–67
[2] de Nalda R, Durá J, García-Vela A, Izquierdo J G, González-Vázquez J and Bañares L 2008 A detailed experimental and theoretical study of the femtosecond A-band photodissociation of CH_3I *J. Chem. Phys.* **128** 244309
[3] Corrales M E, González-Vázquez J, Balerdi G, Solá I R, de Nalda R and Bañares L 2014 Control of ultrafast molecular photodissociation by laser-field-induced potentials *Nat. Chem.* **6** 785
[4] Corrales M E, González-Vázquez J, de Nalda R and Bañares L 2019 Coulomb explosion imaging for the visualization of a conical intersection *J. Phys. Chem. Lett.* **10** 138–43
[5] Murillo-Sánchez M L, González-Vázquez J, Corrales M E, de Nalda R, Martínez-Núñez E, García-Vela A and Bañares L 2020 Femtochemistry under scrutiny: clocking state-resolved channels in the photodissociation of CH_3I in the A-band *J. Chem. Phys.* **152** 014304
[6] Erk B *et al* 2014 Imaging charge transfer in iodomethane upon x-ray photoabsorption *Science* **345** 288–91
[7] Motomura K *et al* 2015 Charge and nuclear dynamics induced by deep inner-shell multiphoton ionization of CH_3I molecules by intense x-ray free-electron laser pulses *J. Phys. Chem. Lett.* **6** 2944–9
[8] Boll R *et al* 2016 Charge transfer in dissociating iodomethane and fluoromethane molecules ionized by intense femtosecond x-ray pulses *Struct. Dyn.* **3** 043207
[9] Graham P *et al* 2001 On the fragment ion angular distributions arising from the tetrahedral molecule CH_3I *J. Phys. B: At. Mol. Opt. Phys.* **34** 4015
[10] Liu H, Yang Z, Gao Z and Tang Z 2007 Ionization and dissociation of CH_3I in intense laser field *J. Chem. Phys.* **126** 044316
[11] Wang Y, Zhang S, Wei Z and Zhang B 2008 Velocity map imaging of dissociative ionization and coulomb explosion of CH_3I induced by a femtosecond laser *J. Phys. Chem.* A **112** 3846–51

[12] Corrales M E, Gitzinger G, González-Vázquez J, Loriot V, de Nalda R and Bañares L 2012 Velocity map imaging and theoretical study of the coulomb explosion of CH$_3$I under intense femtosecond IR pulses *J. Phys. Chem.* A **116** 2669–77

[13] Walt S G, Bhargava Ram N, von Conta A, Tolstikhin O I, Madsen L B, Jensen F and Wörner H J 2015 Role of multi-electron effects in the asymmetry of strong-field ionization and fragmentation of polar molecules: the methyl halide series *J. Phys. Chem.* A **119** 11772–82

[14] Zhang D *et al* 2017 Dissociative ionization and coulomb explosion of CH$_3$I in intense femtosecond laser fields *Eur. Phys. J.* D **71** 148

[15] Wei Z, Li J, Wang L, See S T, Jhon M H, Zhang Y, Shi F, Yang M and Loh Z-H 2017 Elucidating the origins of multimode vibrational coherences of polyatomic molecules induced by intense laser fields *Nat. Commun.* **8** 735

[16] Wei Z, Li J, See S T and Loh Z-H 2017 Spin–orbit state-selective C-I dissociation dynamics of the CH$_3$I$^+$ X electronic state induced by intense few-cycle laser fields *J. Phys. Chem. Lett.* **8** 6067

[17] Luo S *et al* 2017 Multiorbital effects in strong-field ionization and dissociation of aligned polar molecules CH$_3$I and CH$_3$Br *Phys. Rev.* A **96** 063415

[18] Luo S, Hu W, Yu J, Li X, He L, Wang C, Liu F and Ding D 2017 Multielectron effects in the strong field sequential ionization of aligned CH$_3$I molecules *J. Phys. Chem.* A **121** 6547–53

[19] Winney A H, Basnayake G, Debrah D A, Lin Y F, Lee S K, Hoerner P, Liao Q, Schlegel H B and Li W 2018 Disentangling strong-field multielectron dynamics with angular streaking *J. Phys. Chem. Lett.* **9** 2539–45

[20] Malakar Y *et al* 2019 Time-resolved imaging of bound and dissociating nuclear wave packets in strong-field ionized iodomethane *Phys. Chem. Chem. Phys.* **21** 14090–102

[21] Karlsson L, Jadrny R, Mattsson L, Chau F T and Siegbahn K 1977 Vibrational and vibronic structure in the valence electron spectra of CH$_3$X molecules (X = F, Cl, Br, I, OH) *Phys. Scr.* **16** 225

[22] Holland D M P, Powis I, Öhrwall G, Karlsson L and von Niessen W 2006 A study of the photoionisation dynamics of chloromethane and iodomethane *Chem. Phys.* **326** 535–50

[23] Locht R, Dehareng D, Hottmann K, Jochims H W, Baumgärtel H and Leyh B 2010 The photoionization dynamics of methyl iodide (CH$_3$I): a joint photoelectron and mass spectrometric investigation *J. Phys. B: At. Mol. Opt. Phys.* **43** 105101

[24] Goss S P, Morrison J D and Smith D l 1981 A laser-induced photo-dissociation study of CH$_3$I$^+$ and CD$_3$I$^+$ at high-resolution *J. Chem. Phys.* **75** 757–62

[25] Goss S P, McGilvery D C, Morrison J D and Smith D L 1981 The photodissociation of some alkyl iodide cations *J. Chem. Phys.* **75** 1820–8

[26] Chupka W A, Colson S D, Seaver M S and Woodward A M 1983 Photo-dissociation spectrum of CH$_3$I$^+$ prepared by multiphoton ionization *Chem. Phys. Lett.* **95** 171–6

[27] Woodward A M, Colson S D, Chupka W A and White M G 1986 Vibrational analysis of the A–X photodissociation spectrum of CH$_3$I$^+$ *J. Phys. Chem.* **90** 274–8

[28] Marggi Poullain S, Chicharro D V, González-Vázquez J, Rubio-Lago L and Bañares L 2017 A velocity map imaging study of the photodissociation of the methyl iodide cation *Phys. Chem. Chem. Phys.* **19** 7886–96

[29] Tsuda S, Melton C E and Hamill W H 1964 Ionization-efficiency curves for molecular and fragment ions from methane and the methyl halides *J. Chem. Phys.* **41** 689

[30] Eland J H D, Frey R, Kuestler A, Schulte H and Brehm B 1976 Unimolecular dissociations and internal conversions of methyl halide ions *Int. J. Mass Spectrom. Ion Phys.* **22** 155–70

[31] Powis I 1983 The unimolecular dissociation of electronic state-selected methyl-iodide cations *Chem. Phys.* **74** 421–32

[32] Mintz D M and Baer T 1976 Kinetic-energy release distributions for dissociation of internal energy selected CH$_3$I$^+$ and CD$_3$I$^+$ ions *J. Chem. Phys.* **65** 2407–15

[33] Eckstein M, Yang C-H, Kubin M, Frassetto F, Poletto L, Ritze H-H, Vrakking M J J and Kornilov O 2015 Dynamics of N$_2$ dissociation upon inner-valence ionization by wavelength-selected XUV pulses *J. Phys. Chem. Lett.* **6** 419–25

[34] Eckstein M, Yang C-H, Frassetto F, Poletto L, Sansone G, Vrakking M J J and Kornilov O 2016 Direct imaging of transient Fano resonances in N$_2$ using time-, energy-, and angular-resolved photoelectron spectroscopy *Phys. Rev. Lett.* **116** 163003

[35] Ghafur O, Siu W, Johnsson P, Kling M F, Drescher M and Vrakking M J J 2009 A velocity map imaging detector with an integrated gas injection system *Rev. Sci. Instrum.* **80** 033110

[36] Kroll N M and Watson K M 1973 Charged-particle scattering in the presence of a strong electromagnetic wave *Phys. Rev.* A **8** 804–9

[37] Maquet A and Taïeb R 2007 Two-colour IR + XUV spectroscopies: the soft-photon approximation *J. Mod. Opt.* **54** 1847–57

[38] Hummert J, Kubin M, López S D, Fuks J I, Morales F, Vrakking M J J, Kornilov O and Arbó D G 2020 Retrieving intracycle interference in angle-resolved laser-assisted photoemission from argon *J. Phys. B: At. Mol. Opt. Phys.* **53** 154003

[39] Eland J H D and Duerr E J 1998 Dissociation and electron–ion angular distributions in inner-valence photoionisation of CO and N$_2$ *Chem. Phys.* **229** 13–9

[40] Baltzer P, Larsson M, Karlsson L, Wannberg B and Gothe M C 1992 Inner-valence states of N$_2^+$ studied by UV photoelectron-spectroscopy and configuration-interaction calculations *Phys. Rev.* A **46** 5545

[41] Reiher M and Wolf A 2004 Exact decoupling of the Dirac Hamiltonian. I. General theory *J. Chem. Phys.* **121** 2037–47

[42] Reiher M and Wolf A 2004 Exact decoupling of the Dirac Hamiltonian. II. The generalized Douglas–Kroll–Hess transformation up to arbitrary order *J. Chem. Phys.* **121** 10945–56

[43] Widmark P-O, Malmqvist P k and Roos B r O 1990 Density matrix averaged atomic natural orbital (ANO) basis sets for correlated molecular wave functions *Theor. Chim. Acta* **77** 291–306

[44] Roos B O, Lindh R, Malmqvist P-Å, Veryazov V and Widmark P-O 2004 Main group atoms and dimers studied with a new relativistic ANO basis set *J. Phys. Chem.* A **108** 2851–8

[45] Györffy W, Shiozaki T, Knizia G and Werner H-J 2013 Analytical energy gradients for second-order multireference perturbation theory using density fitting *J. Chem. Phys.* **138** 104104

[46] Shiozaki T, Györffy W, Celani P and Werner H-J 2011 Communication: extended multi-state complete active space second-order perturbation theory: energy and nuclear gradients *J. Chem. Phys.* **135** 081106

[47] Shiozaki T 2017 BAGEL: brilliantly advanced general electronic-structure library *Wiley Interdiscip. Rev.-Comput. Mol. Sci.* **8** e1331

[48] Vlaisavljevich B and Shiozaki T 2016 Nuclear energy gradients for internally contracted complete active space second-order perturbation theory: multistate extensions *J. Chem. Theory Comput.* **12** 3781–7

[49] Park J W and Shiozaki T 2017 On-the-fly CASPT2 surface-hopping dynamics *J. Chem. Theory Comput.* **13** 3676–83

[50] Park J W and Shiozaki T 2017 Analytical derivative coupling for multistate CASPT2 theory *J. Chem. Theory Comput.* 2561–70

[51] Schimmelpfennig B 1996 *AMFI, An Atomic Mean-Field Integral Program* (Stock. University)

[52] Fernández Galván I *et al* 2019 OpenMolcas: from source code to insight *J. Chem. Theory Comput.* **15** 5925–64

[53] Neese F 2012 The ORCA program system *Wiley Interdiscip. Rev.-Comput. Mol. Sci.* **2** 73–8

[54] González-Vázquez J 2019 Generator of initial conditions https://github.com/sharcdyn/initialconditions

[55] Richter M, Marquetand P, González-Vázquez J, Sola I and González L 2011 SHARC: *ab initio* molecular dynamics with surface hopping in the adiabatic representation including arbitrary couplings *J. Chem. Theory Comput.* **7** 1253–8

[56] Petersen J and Mitrić R 2012 Electronic coherence within the semiclassical field-induced surface hopping method: strong field quantum control in K_2 *Phys. Chem. Chem. Phys.* **14** 8299–306

[57] Feit M D and Fleck J A Jr 1983 Solution of the Schrödinger equation by a spectral method II: vibrational energy levels of triatomic molecules *J. Chem. Phys.* **78** 301–8

[58] Feit M D and Fleck J A Jr 1984 Wave packet dynamics and chaos in the Hénon–Heiles system *J. Chem. Phys.* **80** 2578–84

[59] Feit M D, Fleck J A Jr and Steiger A 1982 Solution of the Schrödinger equation by a spectral method *J. Comput. Phys.* **47** 412–33